



# Exploring the Cosmological Triangle in Search for Axion-Like Particles from a Reactor

Byung Ju Park,<sup>1,2</sup> Jae Jin Choi,<sup>3,2</sup> Eunju Jeon,<sup>2,1</sup> Jinyu Kim,<sup>4</sup> Kyungwon Kim,<sup>2</sup> Sung Hyun Kim,<sup>2</sup> Sun Kee Kim,<sup>3</sup> Yeongduk Kim,<sup>2,1</sup> Young Ju Ko,<sup>2</sup> Byoung-Cheol Koh,<sup>5</sup> Chang Hyon Ha,<sup>5</sup> Seo Hyun Lee,<sup>1,2</sup> In Soo Lee,<sup>2,\*</sup> Hyunseok Lee,<sup>1,2</sup> Hyun Su Lee,<sup>2,1,†</sup> Jaison Lee,<sup>2</sup> and Yoomin Oh<sup>2</sup>  
(NEON Collaboration)

Doojin Kim,<sup>6,7</sup> Gordan Krnjaic,<sup>8,9,10</sup> and Jacopo Nava<sup>11,12</sup>

<sup>1</sup>*IBS School, University of Science and Technology (UST), Deajeon 34113, Republic of Korea*

<sup>2</sup>*Center for Underground Physics, Institute for Basic Science (IBS), Daejeon 34126, Republic of Korea*

<sup>3</sup>*Department of Physics and Astronomy, Seoul National University, Seoul 08826, Republic of Korea*

<sup>4</sup>*HANARO Utilization Division, Korea Atomic Energy Research Institute (KAERI), Deajeon 34057, Republic of Korea*

<sup>5</sup>*Department of Physics, Chung-Ang University, Seoul 06973, Republic of Korea*

<sup>6</sup>*Department of Physics, University of South Dakota, Vermillion, SD 57069, USA*

<sup>7</sup>*Mitchell Institute for Fundamental Physics and Astronomy,*

*Department of Physics and Astronomy, Texas A&M University, College Station, TX 77845, USA*

<sup>8</sup>*Theoretical Physics Division, Fermi National Accelerator Laboratory, Batavia, IL, USA*

<sup>9</sup>*Department of Astronomy & Astrophysics, University of Chicago, Chicago, IL USA*

<sup>10</sup>*Kavli Institute for Cosmological Physics, University of Chicago, Chicago, IL USA*

<sup>11</sup>*Dipartimento di Fisica e Astronomia, Università di Bologna, via Irnerio 46, 40126, Bologna, Italy*

<sup>12</sup>*INFN, Sezione di Bologna, viale Berti Pichat 6/2, 40127, Bologna, Italy*

(Dated: December 31, 2024)

We report new constraints on axion-like particles (ALPs) using data from the NEON experiment, which features a 16.7 kg of NaI(Tl) target located 23.7 meters from a 2.8 GW thermal power nuclear reactor. Analyzing a total exposure of 3063 kg·days, with 1596 kg·days during reactor-on and 1467 kg·days during reactor-off periods, we compared energy spectra to search for ALP-induced signals. No significant signal was observed, enabling us to set exclusion limits at the 95% confidence level. These limits explore previously inaccessible regions of the ALP parameter space, particularly axion mass ( $m_a$ ) around  $1 \text{ MeV}/c^2$ . For ALP-photon coupling ( $g_{a\gamma}$ ), limits reach as low as  $6.24 \times 10^{-6} \text{ GeV}^{-1}$  at  $m_a = 3.0 \text{ MeV}/c^2$ , while for ALP-electron coupling ( $g_{ae}$ ), limits reach  $4.95 \times 10^{-8}$  at  $m_a = 1.02 \text{ MeV}/c^2$ . This work pioneers reactor-based exploration of the “cosmological triangle” for ALP-photon coupling and demonstrates the potential for future reactor experiments to uncover unexplored ALP parameter space.

## I. INTRODUCTION

Axions are hypothetical particles first proposed in 1977 by Peccei and Quinn [1] to address the strong  $CP$  problem in quantum chromodynamics (QCD) [2, 3]. Due to their extremely light mass and weak interactions with ordinary matter, axions are considered strong candidates for dark matter [4–8]. Despite numerous experimental searches, axions have not yet been detected [9–12]. The concept has since been extended to include axion-like particles (ALPs) in various models [13, 14]. While ALPs share many properties with axions, making them viable dark matter candidates, they are not necessarily tied to solving the strong  $CP$  problem. ALPs can span a wide range of masses and coupling constants, leading to diverse phenomenological implications in astrophysical and laboratory contexts [14].

ALPs interact with Standard Model leptons and the electromagnetic field, driving extensive experimental searches [12]. Light ALPs (masses below  $100 \text{ keV}/c^2$ ) are typically investigated using solar helioscopes, haloscopes, or photon regeneration experiments [15]. In contrast, heavy ALPs (mass above

$100 \text{ keV}/c^2$ ) are probed using colliders or beam dump experiments [16]. Astrophysical observations provide complementary constraints on the ALP parameter space [17, 18]. Notably, a region with ALP masses ( $m_a$ ) around  $0.3\text{--}8 \text{ MeV}/c^2$  and axion-photon coupling constant ( $g_{a\gamma}$ ) of approximately  $1.8 \times 10^{-6}$  to  $5 \times 10^{-5} \text{ GeV}^{-1}$  remains unexplored by direct searches and astrophysical bounds. This region, known as the “cosmological triangle” [19, 20], was previously accessible only through model-dependent cosmological arguments [21, 22]. Growing interest in this region [20] has spurred studies suggesting the potential for ALP searches using short-baseline reactor experiments [23, 24], the accelerator-based CCM experiment with a 10-ton liquid argon target [25], DUNE-like future neutrino experiments with a 50-ton liquid or gaseous argon target [19], and a 2-kton liquid scintillator with an intense proton beam underground [26].

Nuclear reactors are the most intense sources of photons with energies up to a few MeV. Since ALPs can be produced via photon-induced scattering [14], reactors offer a promising avenue for ALP searches in the  $\text{MeV}/c^2$  mass range. However, only a few reactor-based ALP searches have been conducted [27, 28].

In reactor-based ALP searches, data collected during reactor operation (reactor-on data) can be compared to data collected when the reactor is inactive (reactor-off data) to con-

\* islee@ibs.re.kr

† hyunsulee@ibs.re.kr

strain potential ALP signals. Assuming no reactor-operation-related backgrounds, reactor-on minus reactor-off data provides a clean method for identifying ALP signals without dominant background interference. A thorough understanding of time-dependent backgrounds is crucial, as such backgrounds could easily mimic the signals of interest.

In this study, we present a direct search for ALPs using the NEON experiment [29], employing detailed time-dependent background modeling for each NaI(Tl) target crystal. Leveraging the intense ALP production from the reactor core, the NEON experiment, with a modest target mass of 16.7 kg of NaI(Tl) crystals, begins to probe the unexplored “cosmological triangle” in a laboratory-based experiment. For axion-electron couplings, this study investigates previously uncharted parameter space for axion masses between 300 keV/c<sup>2</sup> and 1 MeV/c<sup>2</sup>.

## II. NEON EXPERIMENT

The NEON (Neutrino Elastic scattering Observation with NaI) experiment is designed to detect coherent elastic neutrino-nucleus scattering (CE $\nu$ NS) using reactor electron antineutrinos [29]. The detector is located in the tendon gallery of reactor unit-6 at the Hanbit nuclear power complex in Yeonggwang, Korea. This reactor has a thermal power of 2.8 GW, and the detector is positioned  $23.7 \pm 0.3$  m from the center of the reactor core. This location and distance are similar to those in the NEOS experiment [30], which was installed in reactor unit-5 within the same complex. As the NEOS experiment reported no significant reactor-correlated backgrounds for either  $\gamma$ -rays [31] or neutrons [32], the environmental background at the NEON experimental site is expected to be similar.

After an engineering run in 2021 [29], the detector encapsulation was upgraded to enhance long-term operational stability [33]. Furthermore, two small-size detector modules were replaced with larger modules, resulting in a total crystal mass of 16.7 kg.

The six NaI(Tl) modules are housed within a four-layer nested shielding system comprising a polyethylene castle, a borated polyethylene board, a lead castle, and a linear alkylbenzene-based liquid scintillator [29], as shown in Fig. 1. The six NaI(Tl) crystal assemblies are immersed in 800 liters of liquid scintillator.

Each NaI(Tl) crystal is directly coupled to two photomultiplier tubes (PMTs) without quartz windows to enhance light collection efficiency [33, 34]. The crystal and PMT assemblies are encapsulated in a copper casing [33]. Events that satisfy the trigger condition—coincident photoelectrons detected by both of the crystal’s PMTs within a 200 ns window—are recorded using 500 MHz flash analog-to-digital converters (FADCs). These events are stored as 8  $\mu$ s waveforms, beginning 2.4  $\mu$ s before the trigger [29, 35]. The system records two readouts: a high-gain signal from the anode for the 0–60 keV energy range and a low-gain signal from the fifth-stage dynode for the 60–3000 keV range, similar to the setup used in the COSINE-100 experiment [35]. To mitigate the high trig-

ger rate caused by muon events, an event veto logic applies a 300 ms dead time for energy deposits exceeding approximately 3 MeV in each crystal. This veto logic results in a dead time of approximately 10% for 8-inch crystals and 5% for 4-inch crystals [29]. The muon candidate event rate was monitored, and the exact dead time was evaluated for each hourly dataset.

The data analyzed in this study were collected between April 11, 2022 and June 22, 2023, yielding a total live time exposure of 5702 kg-days. Data collection was generally stable, although downtime occurred due to unexpected power outages. These outages caused failures in the high voltage supply crate and malfunctions in a data acquisition (DAQ) module. To ensure reactor security, the lack of an online connection extended downtime during summer 2022. Despite these challenges, an average DAQ efficiency of approximately 70% was maintained throughout the analyzed data period.

At the start of physics operations, we collected data while the reactor was operating at full power (reactor-on data) for 120 days. However, an unexpected power outage caused the NEON DAQ system to be offline for 38 days during this period. The reactor was inactive from September 26, 2022, to February 22, 2023, for regular maintenance and fuel replacement, during which reactor-off data were collected for 144 days. After maintenance, the reactor resumed operation on February 22, 2023. To avoid complexities arising from changes in photon and ALP fluxes, data from the 3-day ramp-down period (September 23–26) and ramp-up period (February 22–25) were excluded. Once the reactor restarted, it operated stably at full power. Data collected through June 22, 2023, added an additional 117 days of reactor-on exposure.

## III. DATA PROCESS

The energy scales and resolutions were determined through calibration using both internal  $\beta$ - and  $\gamma$ -ray peaks from radioactive contaminants within the crystals and external sources. For external  $\gamma$ -ray calibrations, <sup>241</sup>Am and <sup>22</sup>Na sources, enclosed in stainless-steel cases suitable for the calibration tube, were prepared using standard isotope solutions with activities of approximately 100 Bq. These sources were installed in the calibration holes to provide  $\gamma$ -ray energies of 59.54 keV, 511 keV, and 1275 keV for calibrating both NaI(Tl) crystals and liquid scintillator [29]. Internal radioactive contaminant peaks, including 49 keV (<sup>210</sup>Pb), 238 keV (<sup>212</sup>Pb), 295 and 352 keV (<sup>214</sup>Pb), 1173 keV (<sup>60</sup>Co), 1462 keV (<sup>40</sup>K), 1764 keV and 2204 keV (<sup>214</sup>Bi), and 2614 keV (<sup>208</sup>Tl), were also used to calibrate the NaI(Tl) crystals, following methods similar to those used in the COSINE-100 experiment [36]. Nonlinear crystal responses, as characterized in Refs. [37, 38], were also accounted for during the calibration process.

During offline analysis, events with energy deposits exceeding 5 MeV in the liquid scintillator were rejected as muon candidate events. Additional criteria were applied to exclude muon phosphorus events and electronic interference. These include requiring waveforms from the crystal to exhibit more than two single photoelectrons, ensuring the integral wave-

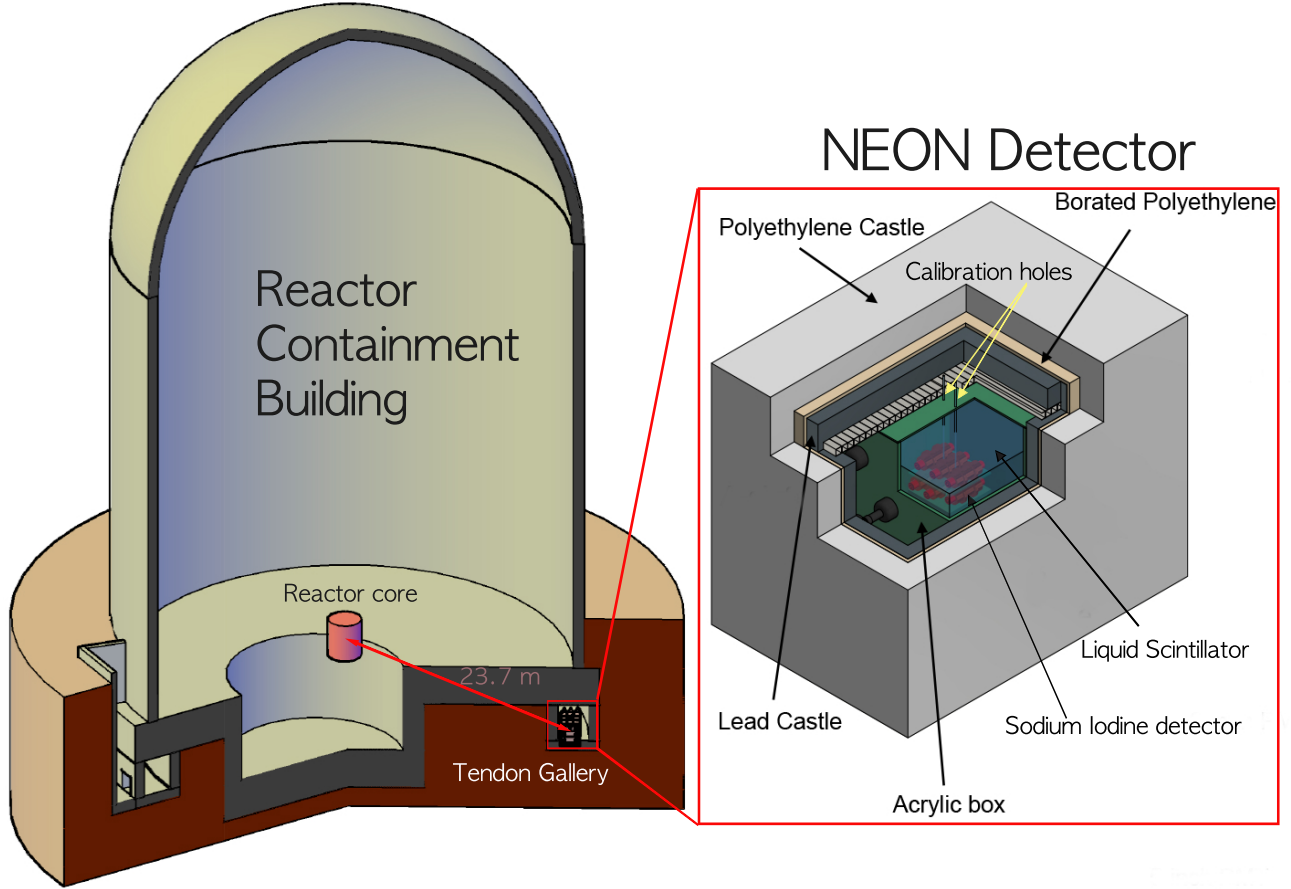


Fig. 1. Schematic view of the NEON detector. The NEON detector is located 23.7 m from the reactor core of unit-6 at the Hanbit nuclear power complex, which operates at a thermal power of 2.8 GW. The detector consists of six NaI(Tl) modules enclosed within 800 L of liquid scintillator, surrounded by a 10 cm-thick lead layer, a 3 cm-thick borated polyethylene layer, and a 20 cm-thick high-density polyethylene shield.

form area below the baseline does not exceed a set limit, and rejecting events where trigger pulse leading edges occur earlier than  $2.0 \mu\text{s}$  after recording begins. Alpha-induced events from uranium or thorium contamination were also excluded by requiring a charge-weighted average time greater than  $2.4 \mu\text{s}$ .

This analysis focused on events with energies between 3 keV and 3000 keV to avoid contamination from unexpected noise. Noise events were effectively removed using a boosted decision tree (BDT)-based event selection algorithm [39]. While this analysis was not significantly affected by low-energy noise, the same data quality cuts developed for low-energy analyses—such as CE $\nu$ NS and low-mass dark matter searches [40]—were applied. The quality of the data was monitored by evaluating event rates in the 1–3 keV range after applying BDT-based event selection criteria. Each one-hour dataset was classified as “good” if its event rate fell within  $3\sigma$  of the mean event rate distribution; otherwise, it was classified as “bad”.

Detector-3 exhibited large fluctuations in low-energy event rates, leading to its exclusion from the ALP search analysis. Table I summarizes the data exposure for each crystal that

passed all selection criteria, and Fig. 2 illustrates these exposures over time for each detector module. In total, this analysis utilized 1596 kg·days of reactor-on data and 1467 kg·days of reactor-off data.

TABLE I. Summary of good quality data. The table provides an overview of the data used for the ALP searches, categorized by detector module and separated into reactor-on and reactor-off periods. Data from detector-3 were excluded from the analysis due to contamination from low-energy noise.

Detector	Mass	reactor-on data	reactor-off data
detector-1	1.67 kg	165.4 kg·days	201.2 kg·days
detector-2	3.34 kg	413.4 kg·days	352.3 kg·days
detector-3	1.67 kg	—	—
detector-4	3.34 kg	527.9 kg·days	367.6 kg·days
detector-5	3.35 kg	160.2 kg·days	279.8 kg·days
detector-6	3.35 kg	329.4 kg·days	266.0 kg·days
Total	16.72 kg	1596.3 kg·days	1466.9 kg·days

Selected events were further categorized as single-hit or

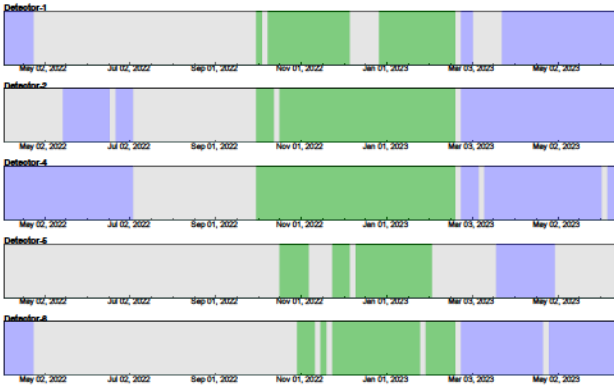


Fig. 2. Good quality data in the time domain. The figure shows good quality data as a function of time for each detector module. Reactor-on data is depicted in blue, reactor-off data in green, and periods of DAQ downtime or poor-quality data are indicated in gray.

multiple-hit events. A multiple-hit event was defined as having accompanying crystal signals with more than four photoelectrons or a liquid scintillator signal exceeding 80 keV within a 150 ns time coincidence window. Events that did not meet these criteria were classified as single-hit samples.

#### IV. TIME DEPENDENT BACKGROUND COMPONENT

The dominant  $^{210}\text{Pb}$  contamination, with a half-life of 22.3 years, exhibits negligible variation over the one-year data period. Therefore, we define effectively time-independent background components as the “Continuum background”, which includes internal contaminants, surface contamination, and external radiation, all with a half-lives equal to or greater than that of  $^{210}\text{Pb}$ . In addition to the continuum background, several time-dependent background components contribute differently to reactor-on and reactor-off data.

The cosmogenic contributions to the NaI(Tl) crystal detectors were extensively studied in the the ANAIS [41, 42] and COSINE [43] experiments. These contributions include isotopes such as  $^{125}\text{I}$ ,  $^{121}\text{Te}$ ,  $^{123m}\text{Te}$ ,  $^{125m}\text{Te}$ ,  $^{127m}\text{Te}$ ,  $^{113}\text{Sn}$ ,  $^{22}\text{Na}$  and  $^3\text{H}$ , which primarily affect energy ranges below 100 keV. Among these, long-lived isotopes such as  $^{22}\text{Na}$  (2.6 years) and  $^3\text{H}$  (12.3 years) persist across all detectors. However, short-lived isotopes with half-lives shorter than one year decayed following the initial installation in December 2020. Notably, the initial data from detector-5 and detector-6 were significantly affected by short-lived cosmogenic isotopes, as these crystals were replaced shortly before the start of physics operations. Detector-1 exhibited relatively high cosmogenic activation due to approximately one year of additional muon exposure during R&D on detector encapsulation. Based on exposure times shown in Fig. 2 and the half-life of each isotope, we modeled the cosmogenic contributions for each detector module.

Another significant source of time-dependent background is the seasonal variation of  $^{222}\text{Rn}$ , which has been reported to

be higher during the summer and lower during the winter [44, 45]. The NEOS experiment [30] measured  $^{222}\text{Rn}$  levels in the tendon gallery using a Radon eye device, confirming this seasonal variation. Initially, the NEON experiment did not include a  $^{222}\text{Rn}$  monitoring device. However, in December 2023, a Radon eye was installed to monitor the  $^{222}\text{Rn}$  levels in the tendon gallery.

The NEON detector includes two calibration holes extending from the top of the shield to the vicinity of the crystal modules, as illustrated in Fig. 1. These calibration holes were exposed to the same levels of  $^{222}\text{Rn}$  as the experimental tunnel. As observed in the NEOS experiment, these seasonal  $^{222}\text{Rn}$  variations likely influenced the background levels recorded in the NEON experiment. Simulated spectra for  $^{222}\text{Rn}$  in the calibration holes revealed that the largest contributions occur within the 100–500 keV range for multiple-hit events (see Fig. 3(A)). Summer data showed significantly elevated rates compared to winter data, predominantly due to seasonal variations in  $^{222}\text{Rn}$ . Since most reactor-off data were collected during winter (as shown in Fig. 2), the seasonal variation in  $^{222}\text{Rn}$  resulted in higher background levels for reactor-on data.

Another time-dependent background component arises from dust contamination in the liquid scintillator. The environmental conditions in the tendon gallery contain a significant amount of dust. The only way to minimize dust contamination was to complete all installations quickly and seal the detector system. However, due to unstable detector conditions observed during engineering run [33], approximately one year was spent upgrading the detector encapsulation and conducting various tests with the detector-1 module. During this period, the liquid scintillator was drained and refilled multiple times, leading to dust contamination. At the beginning of the experiment, the liquid scintillator was refilled, and dust particles may have been suspended throughout the scintillator. Over time, these particles likely settled to the bottom of the scintillator, resulting in a gradual decrease in background rates.

To model time-dependent background contributions, the data were divided into seven time periods, each spanning two months. Each dataset was modeled using known NaI(Tl) background components studied in the COSINE-100 experiment [36, 46, 47] as shown in Fig. 3. In this process, contributions from  $^{222}\text{Rn}$  and dust were extracted as summarized in Fig. 4. The extracted  $^{222}\text{Rn}$  contamination levels from the NEON data showed excellent agreement with NEOS measurements using the Radon eye device.

Based on the time-dependent background analysis for each crystal, background contributions for reactor-on (A) and reactor-off (B) dataset were modeled, as shown in Figs. 5 and 6 for single-hit and multiple-hit data, respectively. Background components were categorized into continuum, cosmogenic,  $^{222}\text{Rn}$ , and dust contributions. The remaining backgrounds in the reactor-on-minus-off dataset were modeled using the time-dependent backgrounds of the cosmogenic isotopes,  $^{222}\text{Rn}$ , and dust, as shown in Figs. 5(C) and 6(C). The measured data align well with the expected background models.

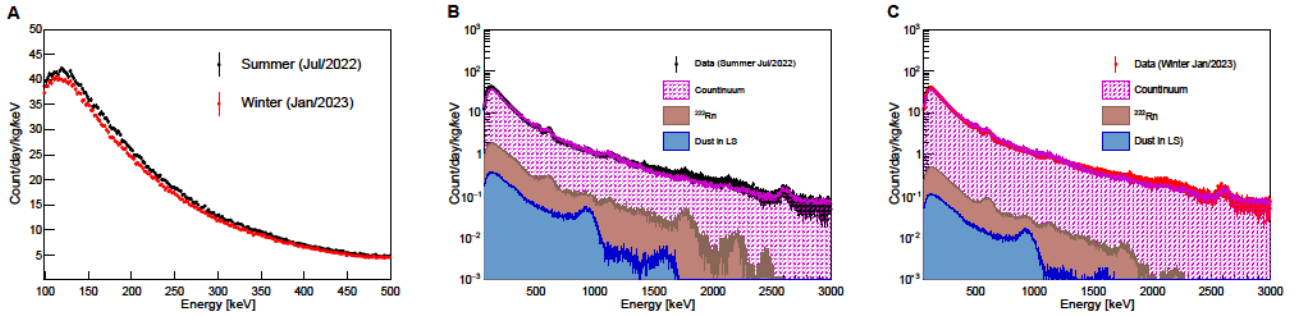


Fig. 3. Time-dependent background models for multiple-hit events in detector-6. Panel (A) shows a noticeable difference in event rates between the summer (15 June 2022 – 15 August 2022) and winter (1 January 2023 – 28 February 2023) seasons, attributed to the seasonal variation of  $^{222}\text{Rn}$ . Panels (B) and (C) illustrate data from summer and winter, respectively, modeled with the time-independent continuum background and time-dependent contributions from  $^{222}\text{Rn}$  and liquid scintillator dust, quantifying the amounts of these components.

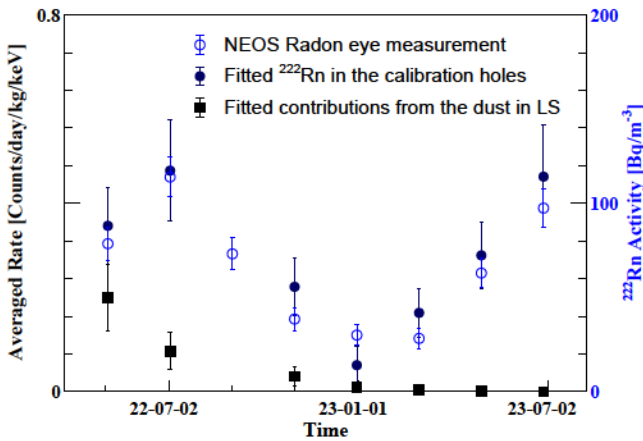


Fig. 4. Time-dependent background contributions from  $^{222}\text{Rn}$  and liquid scintillator dust contamination. The fitted rates for multiple-hit events in detector-6, averaged over energies between 100 keV and 500 keV, are presented (left axis). Contributions include  $^{222}\text{Rn}$  in the calibration holes (dark blue filled circles) and liquid scintillator dust (black filled squares). Measured  $^{222}\text{Rn}$  activities (right axis) from the NEOS tunnel using a Radon Eye device (blue open circles) are also shown, corresponding to the same seasons, although these measurements were conducted in different years and in the tendon gallery of reactor unit-5 (while NEON is located at reactor unit-6). Despite differences in location and year, the seasonal variations of  $^{222}\text{Rn}$  show excellent agreement between the NEOS Radon Eye measurements and the NEON data.

## V. ALP SEARCH DATA WITH SYSTEMATIC UNCERTAINTIES

With a well-constructed model of the expected background and the reactor-on-minus-off spectra, as shown in Figs. 5(C) and 6(C), the data spectra for ALP searches were prepared. To accommodate variations in event rates across different energy ranges, dynamic energy bins were employed, spanning from 57 keV (3–60 keV) to 600 keV (2400–3000 keV), as shown in Figs. 9 and 10.

Multiple sources of systematic uncertainties were ac-

counted for, including those associated with energy resolution, energy scale, and background modeling techniques. These uncertainties were translated into variations in the shape or rate of the reactor-on-minus-off spectra. Maximum variations were assumed by considering opposite-side fluctuations between the reactor-on and reactor-off data, as illustrated for the energy resolution systematic shown in Fig. 7. These uncertainties were incorporated into the ALP signal fit as nuisance parameters, constrained within their respective uncertainty ranges.

The dominant systematic uncertainties arose from the time-dependent background modeling of  $^{222}\text{Rn}$  and liquid scintillator dust contributions. Approximately 30% uncertainties were extracted from the time-dependent background rates, as shown in Fig. 3. In addition to rate variations, potential shape changes due to different locations of  $^{222}\text{Rn}$  contamination were also considered. While the background contribution of  $^{222}\text{Rn}$  was primarily attributed to the calibration holes, it was acknowledged that  $^{222}\text{Rn}$  could diffuse into the liquid scintillator [48]. Variations in the positions of  $^{222}\text{Rn}$  contamination relative to the NaI(Tl) detector modules could result in distinct background spectra, as observed in Fig. 8. These shape variations were incorporated into the systematic uncertainty estimations.

The contributions of liquid scintillator dust were modeled using background spectra generated homogeneously within the liquid scintillator, with rate changes modeled based on two-month data periods. In addition to the 30% rate variations, shape changes arising from different contaminant locations were considered. The liquid scintillator was divided into six distinct regions, from top to bottom, to account for positional variations. The maximum shape differences between these regions were included in the systematic uncertainties.

Figures 9 and 10 compare the reactor-on-minus-off data spectra with the expected background contributions, including their associated systematic uncertainty bands, for all analyzed crystals. As demonstrated, the data spectra are generally well-described by the expected time-dependent backgrounds within their systematic uncertainties, providing a reliable basis for the ALP signal search.

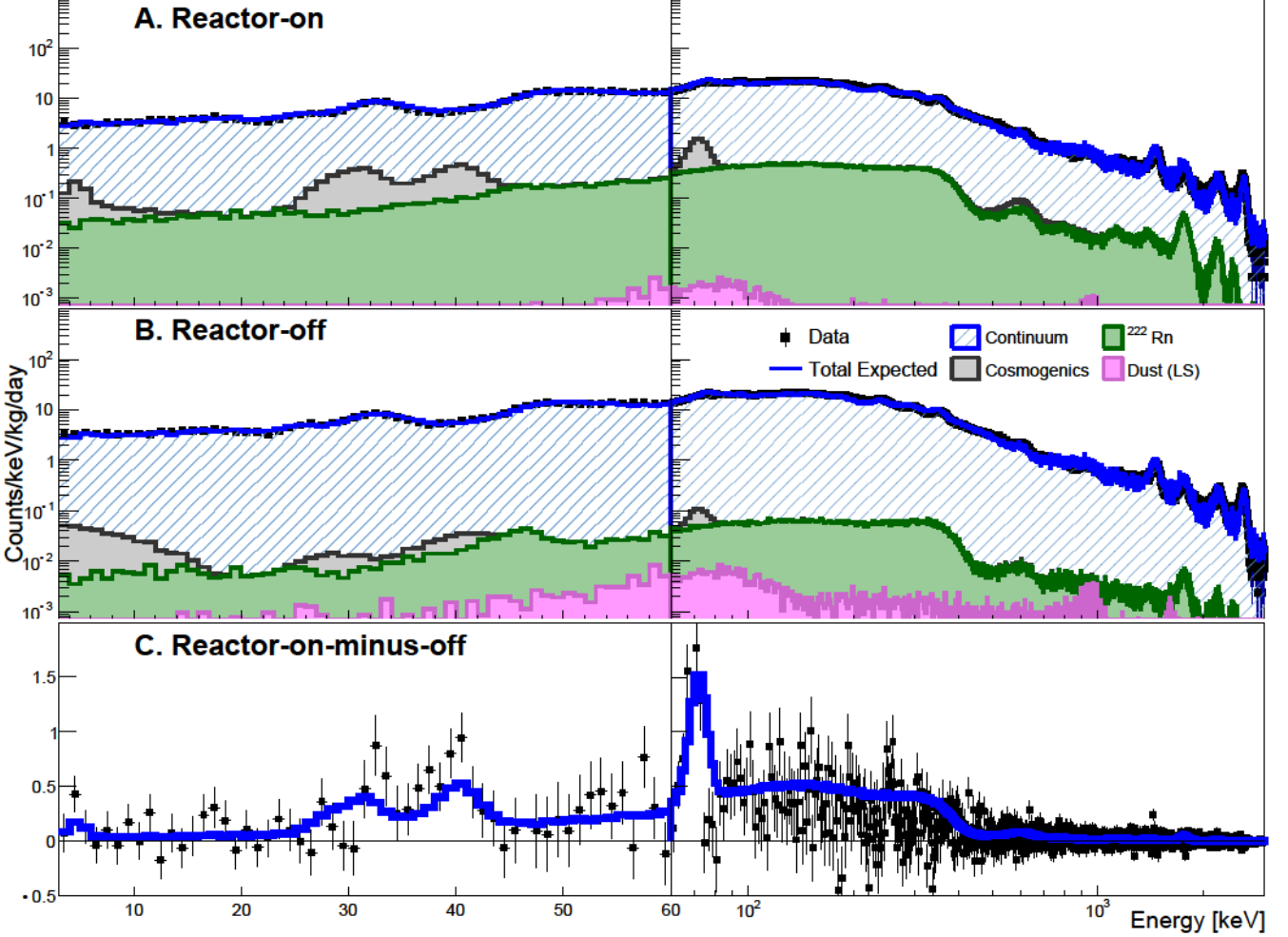


Fig. 5. Single-hit energy spectra of the detector-6 module. The figure shows the normalized energy spectra of single-hit events (black points) in the detector-6 module, compared with the expected background contributions (blue solid lines) for reactor-on data (A), reactor-off data (B), and the reactor-on-minus-off spectrum (C). The expected background includes time-independent continuum components and time-dependent contributions such as cosmogenic activation,  $^{222}\text{Rn}$  in the calibration holes, and  $^{238}\text{U}$  and  $^{232}\text{Th}$  from dust contamination in the liquid scintillator. For the reactor-on-minus-off spectrum (C), only time-dependent components contribute to the background.

## VI. ALP SIGNAL GENERATION

Nuclear reactor cores produce a vast number of photons, which can scatter off fuel materials within the reactor tank to generate ALPs [49]. The photon flux is approximated using the FRJ-1 research reactor model [50], expressed as:

$$\frac{d\Phi_\gamma}{dE_\gamma} = \frac{5.8 \times 10^{17}}{[\text{MeV}] \cdot [\text{sec}]} \left( \frac{P}{[\text{MW}]} \right) e^{-1.1E_\gamma/[\text{MeV}]}, \quad (1)$$

where  $P$  is the thermal power and  $E_\gamma$  is the photon energy. A systematic uncertainty of up to 10% in the photon flux was considered; however, its impact on the derived coupling constants is negligible [24].

We consider a generic model where ALPs couple to photons ( $g_{a\gamma}$ ) or electrons ( $g_{ae}$ ) [51, 52]. ALP production through nuclear de-excitation, as studied by the TEXONO experiment [27], is not considered in this analysis. ALPs can be

produced via the Primakoff process ( $\gamma + A \rightarrow a + A$ ) [53] and the Compton-like process ( $\gamma + e^- \rightarrow a + e^-$ ) [24]. After production in the reactor core, ALPs propagate through shielding materials, either decaying in flight or reaching the detector. The ALP flux at the detector is described as:

$$\frac{d\Phi_a^P}{dE_a} = P_{\text{surv}} \int_{E_{\gamma,\min}}^{E_{\gamma,\max}} \frac{1}{\sigma_{SM} + \sigma_{P(C)}^P} \frac{d\sigma_{P(C)}^P}{dE_a}(E_\gamma, E_a) \times \frac{d\Phi_\gamma}{dE_\gamma}, \quad (2)$$

where  $\sigma_{SM}$  is the total photon scattering cross-section against core material, referenced from the Photon Cross Sections Database [54],  $E_a$  is the energy of the ALP, and  $\sigma_{P(C)}^P$  is the production cross-section for the Primakoff process (Compton-like process) [24].

The ALP survival probability  $P_{\text{surv}}$  to the detector is given

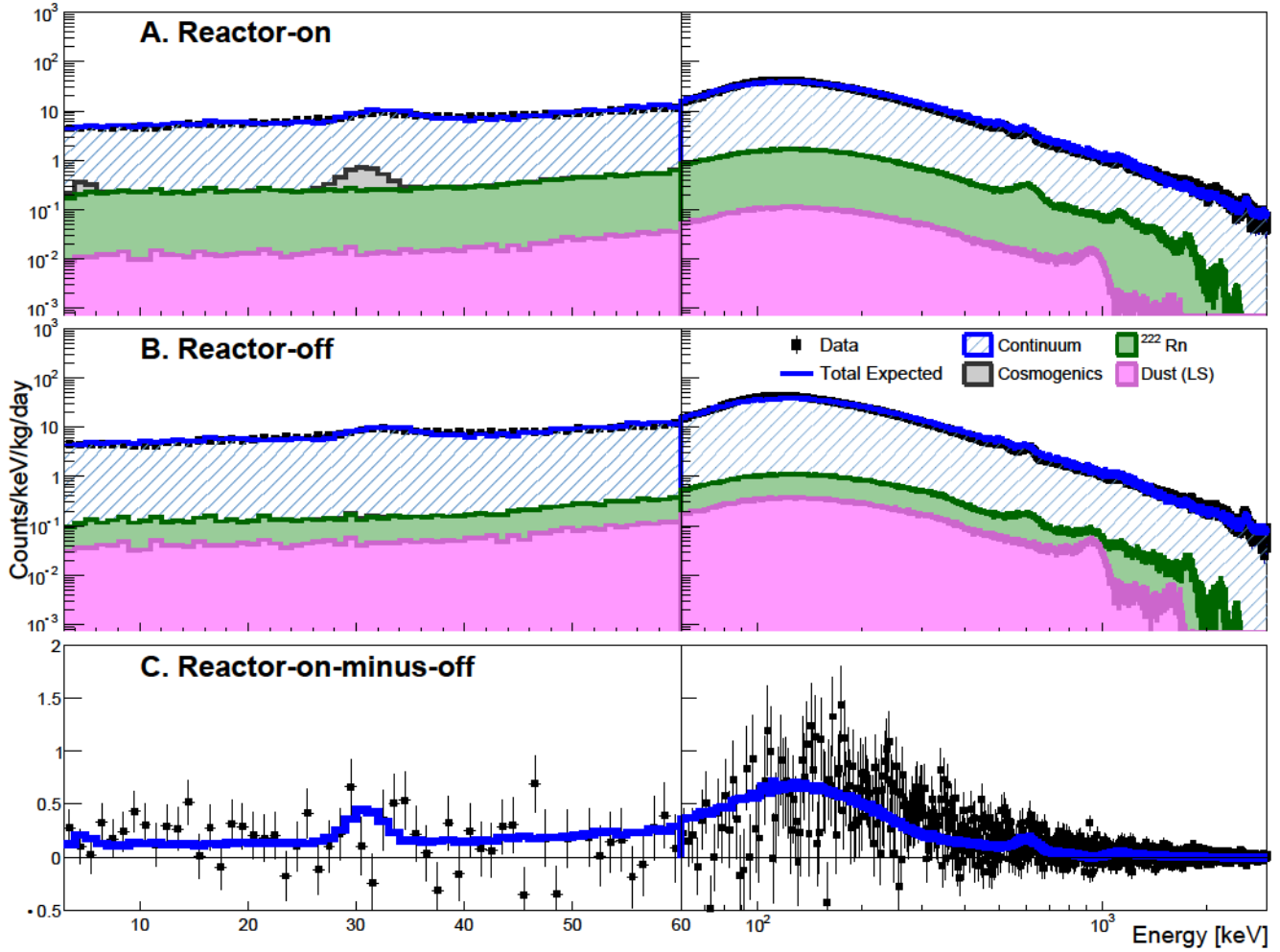


Fig. 6. Multiple-hit energy spectra of the detector-6 module. The figure shows the normalized energy spectra of single-hit events (black points) in the detector-6 module, compared with the expected background contributions (blue solid lines) for reactor-on data (A), reactor-off data (B), and the reactor-on-minus-off spectrum (C). The expected background includes time-independent continuum components and time-dependent contributions such as cosmogenic activation,  $^{222}\text{Rn}$  in the calibration holes, and  $^{238}\text{U}$  and  $^{232}\text{Th}$  from dust contamination in the liquid scintillator. For the reactor-on-minus-off spectrum (C), only time-dependent components contribute to the background.

by [23],

$$P_{\text{surv}} = e^{-LE_a/p_a\tau}, \quad (3)$$

where  $L$  is the distance from the reactor core to the detector,  $p_a$  is the ALP momentum, and  $\tau$  is the ALP lifetime. The lifetime is determined by the decay widths:

$$\Gamma(a \rightarrow \gamma\gamma) = \frac{g_{a\gamma}^2 m_a^3}{64\pi} \quad (4)$$

$$\Gamma(a \rightarrow e^+e^-) = \frac{g_{ae}^2 m_a}{8\pi} \sqrt{1 - 4\frac{m_e^2}{m_a^2}}, \quad (5)$$

where  $m_a$  and  $m_e$  are the ALP and electron masses, respectively.

In case of non-zero  $g_{a\gamma}$ , the ALPs could be detected through the inverse Primakoff process ( $a + A \rightarrow \gamma + A$ ) or

two photon pair decay ( $a \rightarrow \gamma\gamma$ ) in the detector material. The expected signal rate for this process is given by:

$$\frac{dN_{a\gamma}}{dE_a} = \frac{N_{\text{target}}}{4\pi L^2} \sigma_D^P \frac{d\Phi_a^P}{dE_a} + \frac{A}{4\pi L^2} \frac{d\Phi_a^P}{dE_a} P_{\text{decay}}, \quad (6)$$

where  $N_{\text{target}}$  is the number of target nuclei and  $\sigma_D^P$  is the total inverse-Primakoff scattering cross section.  $A$  is the detector transverse area, and  $P_{\text{decay}}$  is the probability of decay within the detector:

$$P_{\text{decay}} = 1 - e^{-L_{\text{det}} E_a / |p_a| \tau}, \quad (7)$$

where  $L_{\text{det}}$  is the detector length in ALP flight direction.

In case of non-zero  $g_{ae}$ , the ALPs could be detected through the inverse-Compton-like process ( $a + e^- \rightarrow \gamma + e^-$ ), Axioelectric absorption ( $a + e^- + N \rightarrow e^- + N$ ) [55], or electron-positron pair decay ( $a \rightarrow e^+e^-$ ). The expected signal rate for

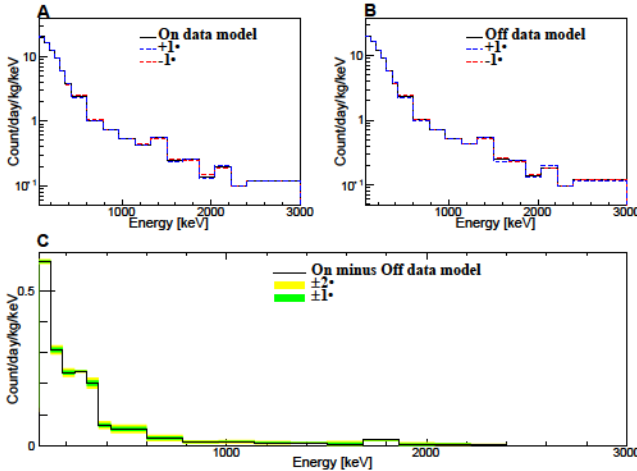


Fig. 7. Systematic uncertainty due to energy resolution. Uncertainty in energy resolution, derived from internal or external  $\gamma$  lines, is propagated into the best-fit model (solid line) of single-hit events for detector-6 across the energy range of 60–3000 keV, as indicated by dashed lines. Variations in the reactor-on data (A) and reactor-off data (B) are carried over into reactor-on-minus-off data spectrum (C), with maximum deviations represented by green ( $1\sigma$ ) and yellow ( $2\sigma$ ) uncertainty bands.

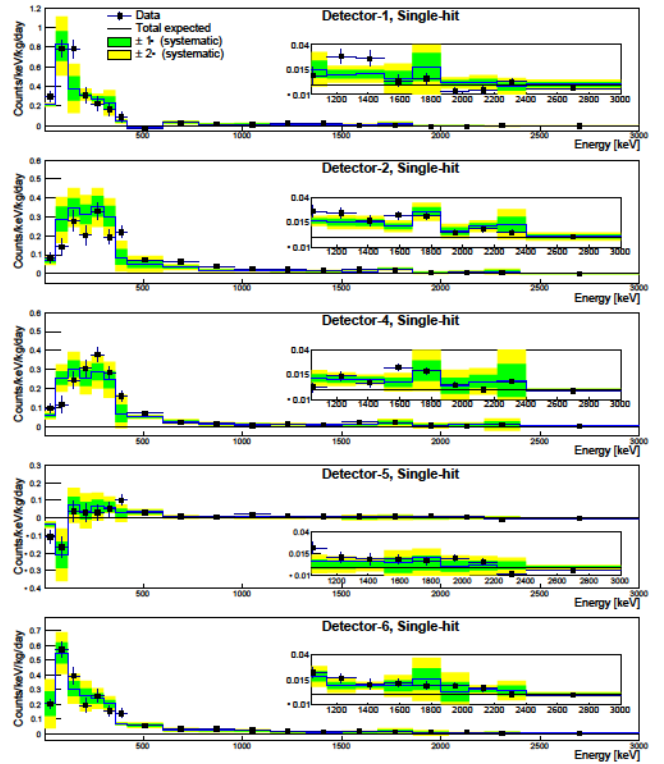


Fig. 9. Single-hit ALP search data. The figure presents the single-hit energy spectra of the reactor-on-minus-off data used for ALP signal searches in the NEON experiment. Data points (black circles) and expected background spectra (blue solid lines) are derived from the models discussed earlier, as shown for the detector-6 module in Fig. 5, but with different bin sizes applied for this analysis. The green and yellow bands represent 68% and 95% confidence level intervals for the background model, respectively. The inset zooms in on the high-energy region for improved visibility.

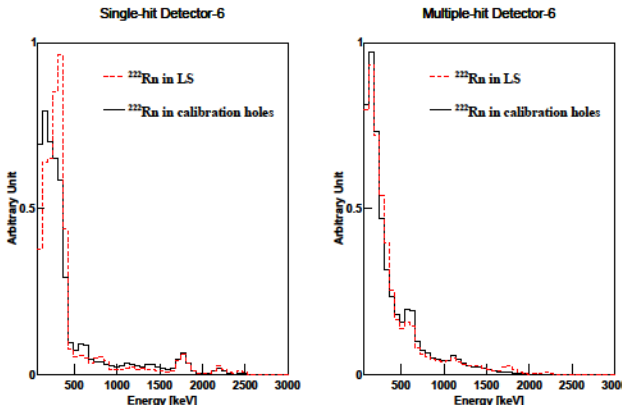


Fig. 8. Systematic uncertainty of  $^{222}\text{Rn}$  shape. Normalized background spectra for the detector-6 module, originating from  $^{222}\text{Rn}$ , are shown separately for single-hit and multiple-hit events. The spectra compare two different locations: the calibration holes and the liquid scintillator. The observed shape differences are treated as systematic uncertainties for  $^{222}\text{Rn}$ , in addition to a 30% rate variation.

this is given by:

$$\frac{dN_C^C}{dE_a} = \frac{N_{\text{target}}}{4\pi L^2} \sigma_D^C \frac{d\Phi_a^C}{dE_a} + \frac{N_{\text{target}}}{4\pi L^2} \sigma_D^A \frac{d\Phi_a^C}{dE_a} + \frac{A}{4\pi L^2} \frac{d\Phi_a^P}{dE_a} P_{\text{decay}}, \quad (8)$$

where  $\sigma_D^C$  and  $\sigma_D^A$  are the inverse-Compton-like process cross section and the Axio-electron cross section, respectively [24, 56].

Figure 11 shows the expected event rates in the NaI(Tl) crystals for various detection processes. These energy spectra account for the total energy of produced standard model particles such as electrons, positrons, and photons in the NaI(Tl) crystals during ALP interactions.

ALP signals for each detection process in the mass range from  $1\text{ eV}/c^2$  to  $10\text{ MeV}/c^2$  were simulated. Calculated ALP fluxes in the reactor were generated isotropically within the reactor core volume, utilizing the geometry shown in Fig. 1 to account for the direction and momentum of ALP events. Upon reaching the detector volume, which includes the liquid scintillator and NaI(Tl) crystals, ALP interactions were simulated, considering both scattering and decay processes for detector responses using Geant4-based simulations. Figure 12 illustrates the expected ALP signals for a few benchmark scenarios in single-hit (A) and the multiple-hit (B) events.

Typically, the  $a \rightarrow e^+e^-$  and axio-electric processes produce electrons and positrons in the detector with energies below a few MeV. In such cases, most of the energy is absorbed by a single detector, resulting in single-hit events. Other processes, such as those involving MeV-energy photons, can de-

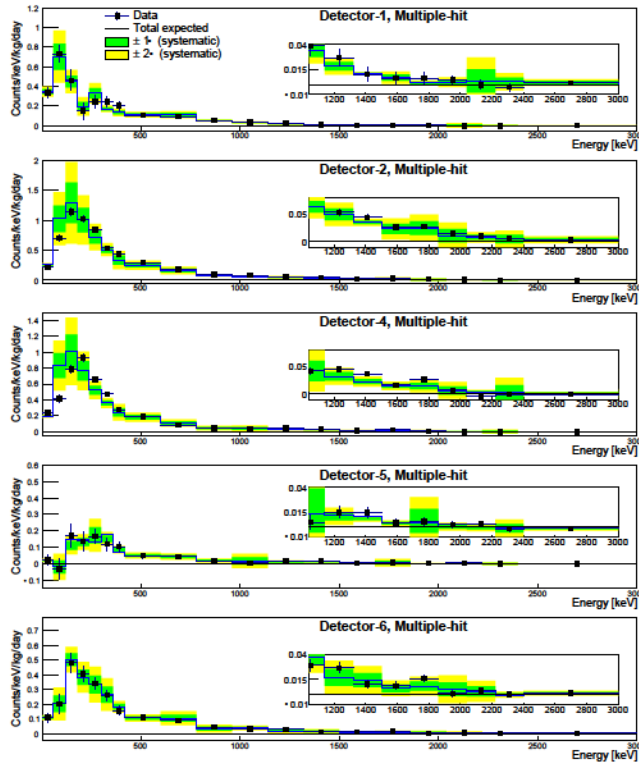


Fig. 10. Multiple-hit ALP search data. The figure presents the single-hit energy spectra of the reactor-on-minus-off data used for ALP signal searches in the NEON experiment. Data points (black circles) and expected background spectra (blue solid lines) are derived from the models discussed earlier, as shown for the detector-6 module in Fig. 6, but with different bin sizes applied for this analysis. The green and yellow bands represent 68% and 95% confidence level intervals for the background model, respectively. The inset zooms in on the high-energy region for improved visibility.

posit energy across multiple detectors through Compton scattering, leading to multiple-hit events, as shown in Fig. 12. Consequently, both single-hit and multiple-hit events are included in the ALP search analysis.

## VII. ALP SIGNAL SEARCHES

The NEON data presented in Figs. 9 and 10 were fitted for each ALP mass and interaction type. Simulated ALP signals were used to evaluate their potential contributions to the measured energy spectra. A  $\chi^2$  fit was applied to the measured spectra for both single-hit and multiple-hit channels in the energy range of 3 to 3,000 keV for each ALP signal and mass. Each crystal and channel were fitted with a crystal-channel-specific background model and a crystal-channel-correlated ALP signal. The combined fit was achieved by summing the  $\chi^2$  values from the five crystals and two channels.

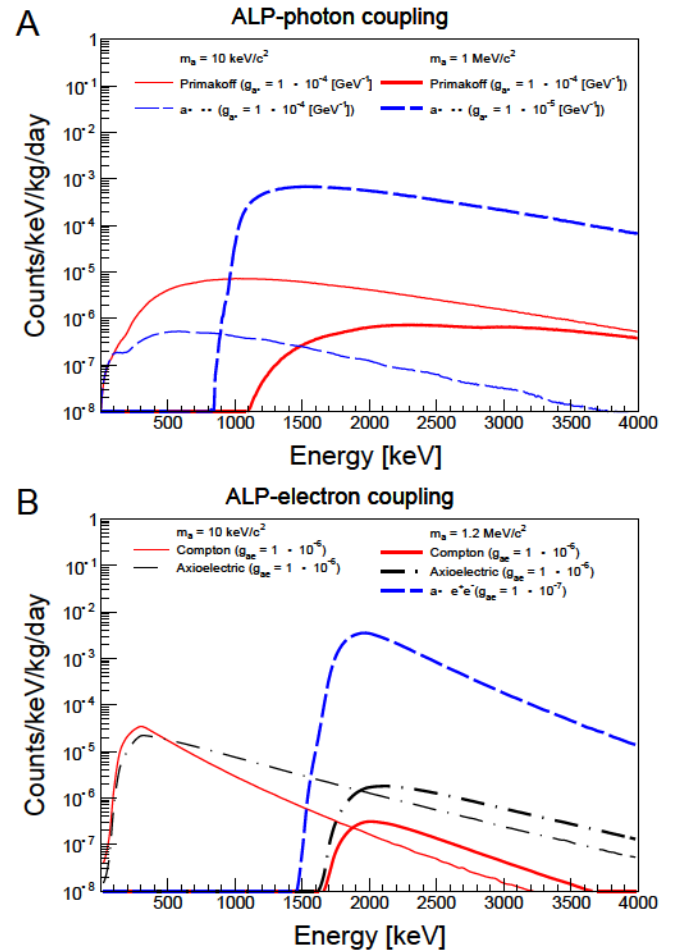


Fig. 11. Expected ALP events rates for each detection process. The scatter and decay rates from axion-photon coupling (A) and axion-electron coupling (B) in the NaI(Tl) crystal are shown for selected values of  $g_{a\gamma}$  and  $g_{ae}$ , corresponding to ALP masses of  $10 \text{ keV}/c^2$ ,  $1 \text{ MeV}/c^2$ , and  $1.2 \text{ MeV}/c^2$ . The total energy of the produced standard model particles is presented.

The  $\chi^2$  fit was performed using the following function:

$$\chi^2 = \sum_i^{10} \sum_j \frac{\left[ M_{ij}(\tau_i^{on}, \tau_i^{off}) - B_{ij}(\alpha, \beta) - S_{ij}(\alpha, m_a) \right]^2}{\sigma_{ij}(\tau_i^{on}, \tau_i^{off})}, \quad (9)$$

where the index  $i$  represents the crystal and channel (single-hit and multiple-hit) numbers, and  $j$  denotes the energy bin.  $M_{ij}(\tau_i^{on}, \tau_i^{off})$  is the normalized rate of reactor-on data subtracted by reactor-off data for crystal (and channel)  $i$  in the  $j^{\text{th}}$  energy bin, scaled by the reactor-on period  $\tau_i^{on}$  and reactor-off period  $\tau_i^{off}$ .  $B_{ij}(\alpha, \beta)$  represents the background, and  $S_{ij}(\alpha, m_a)$  corresponds to ALP signal. The associated uncertainty  $\sigma_{ij}(\tau_i^{on}, \tau_i^{off})$  was propagated from the data collected during the reactor-on and reactor-off periods.

Systematic uncertainties affecting the background model were included as nuisance parameters  $\alpha$  and  $\beta$ . The back-

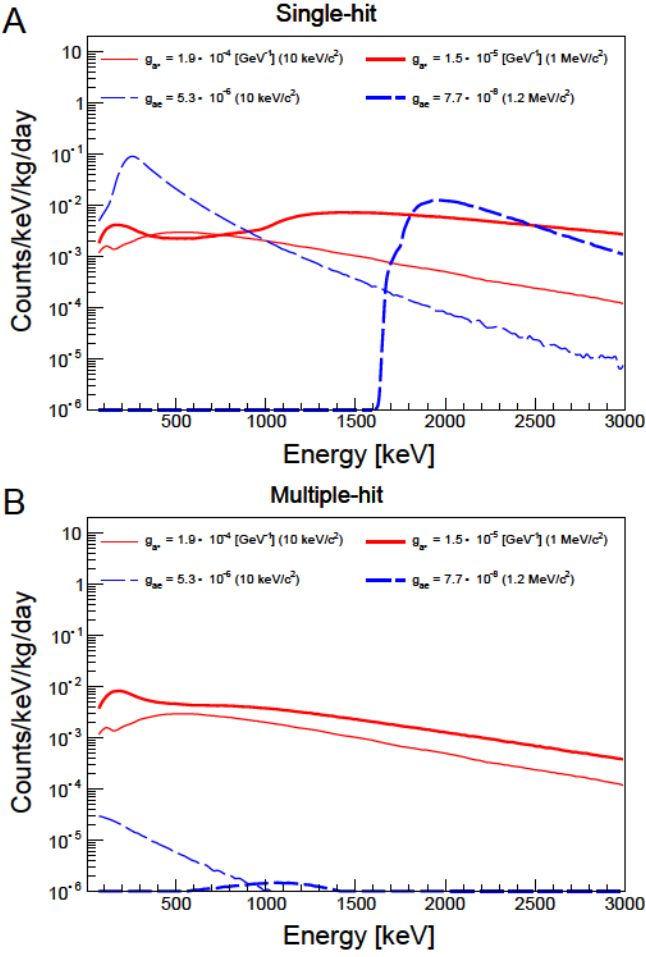


Fig. 12. Expected ALP signals in the NEON detector. The expected event rates from ALP interactions in the NEON detector, incorporating detector responses, are presented for single-hit events (A) and multiple-hit events (B). Selected values of  $g_{a\gamma}$  and  $g_{ae}$  are shown for ALP masses of  $10 \text{ keV}/c^2$ ,  $1 \text{ MeV}/c^2$ , and  $1.2 \text{ MeV}/c^2$ .

ground model is defined as:

$$B_{ij}(\alpha, \beta) = \prod_k (1 + \alpha_{ik} \cdot \delta b_{ijk}) \sum_l (1 + \beta_{il}) B_{ijl}^{MC}, \quad (10)$$

where the index  $k$  represents systematic uncertainty components, and  $l$  denotes the background components.  $B_{ijl}^{MC}$  is the number of background events obtained from modeling for the  $l^{\text{th}}$  background component. The nuisance parameter  $\alpha_{ik}$  controls the energy-dependent uncertainty ( $\delta b_{ijk}$ ), while  $\beta_{il}$  adjusts the activity of the  $l^{\text{th}}$  background component.

The ALP signal model is expressed as:

$$S_{ij}(\alpha, m_a) = \prod_k (1 + \alpha_{ik} \cdot \delta b_{ijk}) S_{ij}(m_a), \quad (11)$$

where the  $S_{ij}(m_a)$  is the expected rate of ALP-photon or ALP-electron interactions in the  $j^{\text{th}}$  energy bin for the  $i^{\text{th}}$  crystal (and channel), as determined from detector simulations. Each nuisance parameter was constrained within its evaluated uncertainty using a Gaussian prior.

For each ALP interaction signal, the probability density function (PDF) was estimated using a raster scan [57] defined as:

$$\text{PDF} = N e^{-(x^2 - \chi_{min}^2)/2}, \quad (12)$$

where  $N$  is a normalization constant ensuring the PDF integrates to unity, and  $\chi_{min}^2$  is the minimum  $\chi^2$ . If the most probable value is consistent with a null signal, a 95% confidence level exclusion limit was obtained by integrating the PDF to 0.95. Figure 13 illustrates an example exclusion limit for  $m_a = 1 \text{ MeV}/c^2$  of axion-photon coupling.

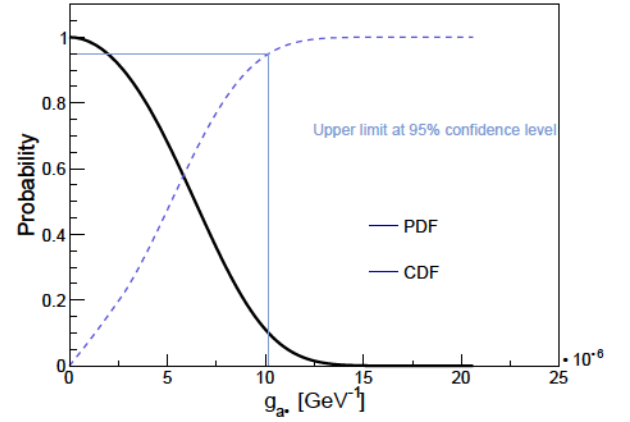


Fig. 13. An example of the probability density function (PDF) and cumulative density function (CDF) for the ALP signal fit with axion-photon coupling at  $m_a = 1 \text{ MeV}/c^2$ . The most probable value corresponds to a null signal, and the 95% confidence level upper limit, determined by the CDF value at 0.95, is  $1.03 \times 10^{-5} \text{ GeV}^{-1}$ .

An example  $\chi^2$  fit for axion-photon coupling with an ALP mass of  $m_a = 1 \text{ MeV}/c^2$  is shown in Fig. 14 for single-hit (A) and multiple-hit (B) events. The averaged energy spectra for the five crystals are displayed along with the best-fit results. For comparison, expected signals for  $m_a = 1 \text{ MeV}/c^2$ ,  $g_{a\gamma} = 1.53 \times 10^{-5} \text{ GeV}^{-1}$  and  $m_a = 10 \text{ keV}/c^2$ ,  $g_{ae} = 5.35 \times 10^{-6}$ , which corresponds to approximately 5 times the signal rates of the 95% confidence level upper limits are included. No statistically significant excess of events was observed for any of the considered ALP signals. Posterior probabilities for all signals were consistent with zero, and 95% confidence level limits were determined.

## VIII. RESULTS AND DISCUSSION

Figure 15 presents the 95% confidence level exclusion limit derived from NEON data for ALPs coupled solely to photons. This limit is shown in the two-dimensional parameter space of ALP mass ( $m_a$ ) and ALP-photon coupling constant ( $g_{a\gamma}$ ). For ALP masses below  $20 \text{ keV}/c^2$ , the dominant contribution arises from the scattering process via the inverse Primakoff process. At higher ALP masses, the limit is set by the

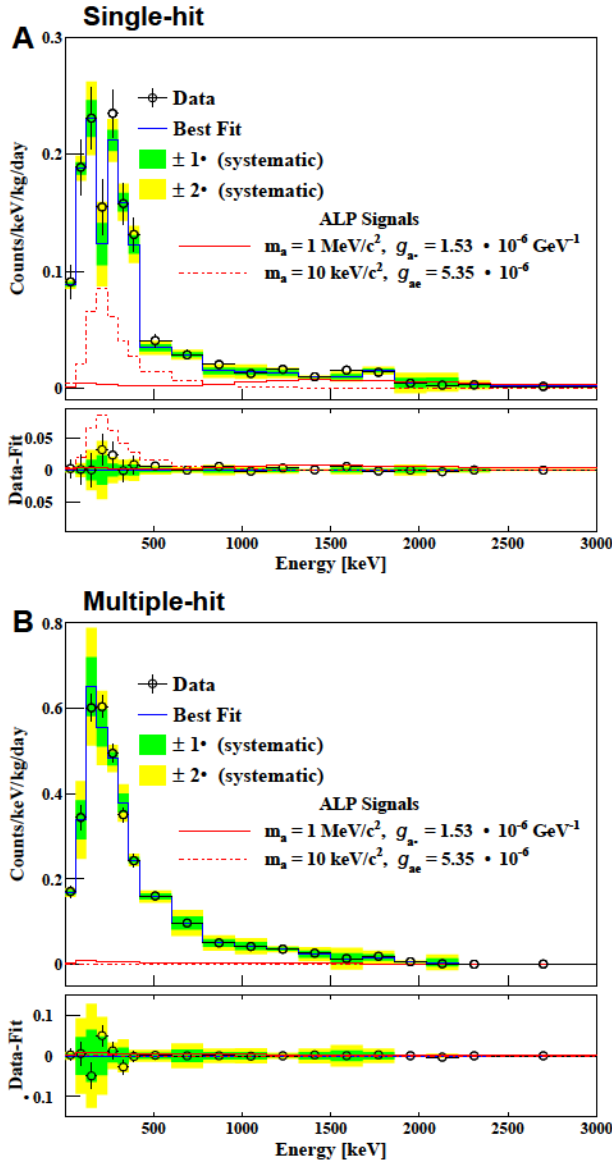


Fig. 14.  $\chi^2$  fit results for axion-photon coupling of  $m_a = 1 \text{ MeV}/c^2$ . The data points (black circles with error bars) represent the summed energy spectra from the five crystals for the normalized reactor-on-minus-off data. The blue solid lines indicate the best-fit results for the  $1 \text{ MeV}/c^2$  ALP mass, assuming axion-photon coupling. Panel (A) corresponds to single-hit events, and panel (B) corresponds to multiple-hit events. The expected signal rates for  $m_a = 1 \text{ MeV}/c^2$  and  $g_{ae} = 1.53 \times 10^{-5} \text{ GeV}^{-1}$  and a  $m_a = 10 \text{ keV}/c^2$  mass and  $g_{ae} = 5.35 \times 10^{-6}$ , which are 5 times higher than the 95% confidence level upper limits of  $g_{ae} = 1.03 \times 10^{-5} \text{ GeV}^{-1}$  and  $g_{ae} = 3.58 \times 10^{-6}$ , are shown as red solid and red dashed lines, respectively. The green and yellow bands represent the 68% and 95% confidence level intervals for the background model fits, respectively. The lower panels display the data minus best-fit residuals.

$a \rightarrow \gamma\gamma$  decay process. Since this decay can occur during the 23.7 meters flight path, limit is considered for both lower and higher  $g_{ae}$  values. The sensitivity of the search decreases for

ALP masses exceeding approximately  $3 \text{ MeV}/c^2$ , primarily due to the limited energy range (up to 3 MeV) of our analysis, which is constrained by detector saturation for high-energy events and reduced photon flux at higher energies. However, signatures of Compton scattering could still allow searches for higher-mass ALPs. In this process, a high-energy photon interacts with the ALP, depositing a lower-energy electron or photon within the detectable range. Future improvements, such as reconstructing saturated events—similar to techniques employed in the COSINE-100 experiment for boosted dark matter searches [58]—could enhance sensitivity to higher-mass ALPs.

The exclusion limits shown in Fig. 15 extend beyond previously unexplored regions of ALP parameter space, surpassing existing constraints from beam dump experiments and astrophysical and cosmological limits as adapted from Refs. [59, 60]. Notably, this study starts to probe the “cosmological triangle”, a previously unconstrained region between beam dump experiments and astrophysical bounds. A small remained region of the KSVZ QCD axion model parameter space [61], corresponding to axion masses of a few  $100 \text{ keV}/c^2$ , is partially ruled out. The exclusion limit reach lower  $g_{ae}$  values, down to  $6.24 \times 10^{-6}$  for  $m_a = 3.0 \text{ MeV}/c^2$ . Compared with a recent reactor-based ALP search using CsI(Tl) crystals [28], the NEON experiment achieved a significantly improved lower bound for  $g_{ae}$ , owing to the larger exposure and lower background levels of the NaI(Tl) crystals. However, the greater distance from the reactor core to the NEON detector results in a reduced upper bound.

Figure 16 displays the 95% confidence level exclusion limit for ALPs coupled purely to electrons, presented in the  $m_a$ – $g_{ae}$  parameter space. For ALP masses below  $1.02 \text{ MeV}/c^2$ , the limit is primarily set by scattering processes via the inverse Compton-like process and axio-electric absorption. For higher ALP masses ( $m_a > 1.0 \text{ MeV}/c^2$ ), the limit is dominated by the  $a \rightarrow e^+e^-$  decay process, which has a kinematic threshold of  $m_a > 2m_e = 1.02 \text{ MeV}/c^2$  (where  $m_e$  is the electron mass). Similar to the ALP-photon case, limits are considered for both upper and lower bounds due to potential ALP decay during flight.

The NEON data also explore previously examined regions constrained by stellar cooling arguments [17] for axion masses below  $300 \text{ keV}/c^2$ , where environmental effects could allow circumvention of these limits [24]. In the mass range of  $300 \text{ keV}/c^2$  and  $1.02 \text{ MeV}/c^2$ , scattering processes probe coupling values down to  $g_{ae}$  about  $3 \times 10^{-6}$ , which were previously unexplored by direct searches or astrophysical and cosmological considerations. This limit extends into regions predicted by the DFSZ-I QCD axion model [61]. For ALP masses above the kinematic limit for  $a \rightarrow e^+e^-$  ( $m_a > 1.02 \text{ MeV}/c^2$ ), the NEON data compete with limits from beam dump experiments [68–70]. The exclusion limit reach lower  $g_{ae}$  values, down to  $4.95 \times 10^{-8}$  for  $m_a = 1.02 \text{ MeV}/c^2$ . The search for axion-electron coupling using NEON data is currently limited to ALP masses below  $1.6 \text{ MeV}/c^2$  due to the 3 MeV dynamic range of the analysis. Similar to the ALP-photon case, reconstructing saturated events above 3 MeV energies could extend the search

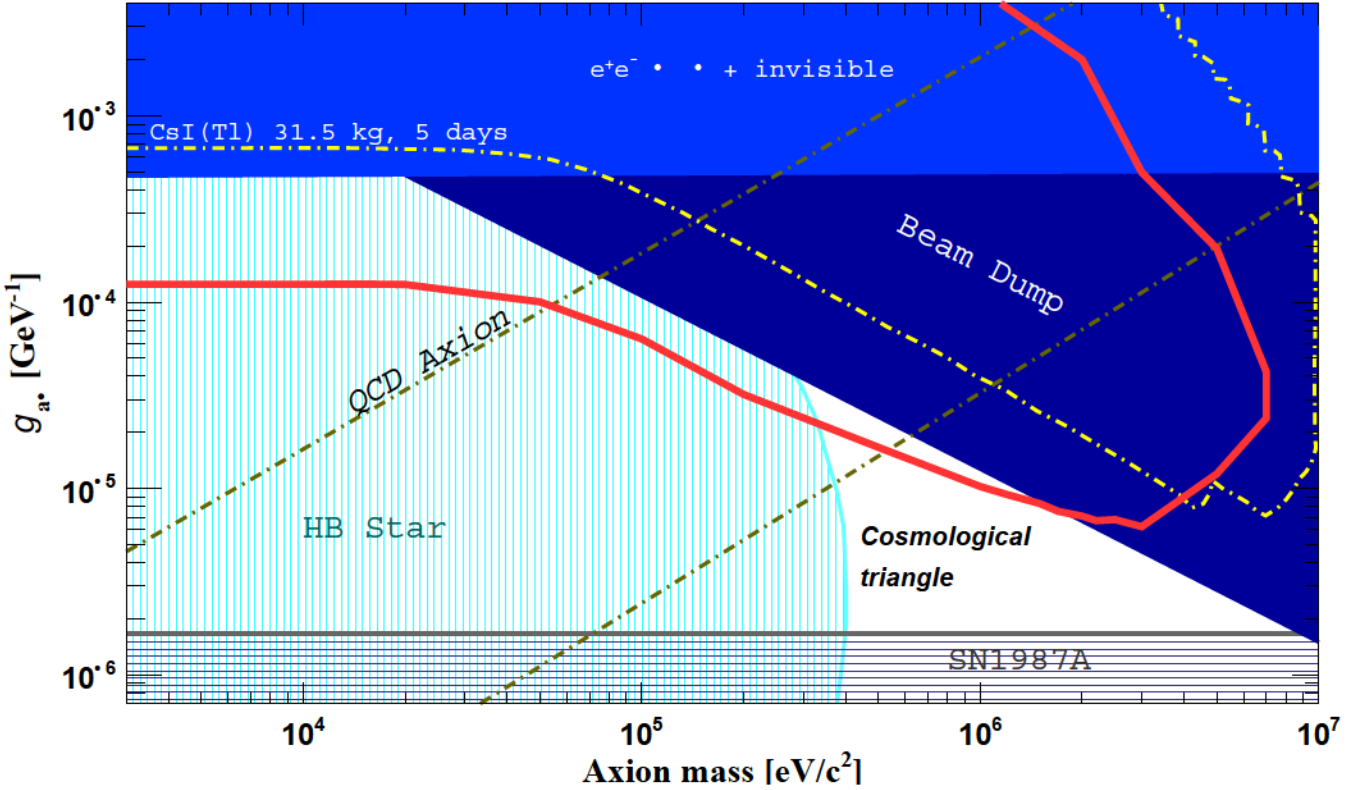


Fig. 15. Exclusion limit on the axion-photon coupling. The observed 95% confidence level exclusion limit (red solid line) derived from NEON data for the axion-photon is compared with limits from beam dump experiments [62, 63], SN1987A [64, 65],  $e^+e^- \rightarrow \gamma + \text{invisible}$  states [66], HB stars cooling arguments [67], and CsI(Tl) exposure in a nuclear reactor [28]. The QCD axion model parameter space for the KSVZ benchmark scenario is indicated by the gray dashed lines [61]. This limit partially covers the remained QCD axion parameter space and the previously unconstrained “cosmological triangle”.

to higher ALP masses, as demonstrated in Refs. [24, 28].

## IX. CONCLUSION

This study reports a direct search for axion-like particles (ALPs) using the NEON experiment, marking a significant step in reactor-based particle physics research. Leveraging 16.7 kg of NaI(Tl) crystals located 23.7 meters from a 2.8 GW thermal power reactor core, NEON has set new exclusion limits for ALPs coupling to photons and electrons. These results probe previously inaccessible regions of ALP parameter space, particularly axin mass around  $1 \text{ MeV}/c^2$ , and provide the first constraints within the “cosmological triangle” for ALP-photon couplings, a region that remained unconstrained until now.

The success of this work stems from the intense photon flux generated by the reactor, precise modeling of background components, and the experiment’s sensitivity to low event rates in signal regions. These findings not only extend the boundaries of ALP research but also demonstrate the capability of reactor-based experiments to probe fundamental particle interactions.

Future advancements, including continued data collection, lowering the energy threshold for coherent elastic neutrino-nucleus scattering (CE $\nu$ NS) searches, and reconstructing events above 3 MeV, promise to further enhance the sensitivity of NEON to ALP signals. Such developments could provide even tighter constraints on ALP properties and open new avenues for understanding beyond-standard-model physics.

## ACKNOWLEDGMENTS

We thank the Korea Hydro and Nuclear Power (KHNP) company for the help and support provided by the staff members of the Safety and Engineering Support Team of Hanbit Nuclear Power Plant 3 and the IBS Research Solution Center (RSC) for providing high performance computing resources. This work is supported by the Institute for Basic Science (IBS) under Project Code IBS-R016-A1 and the National Research Foundation (NRF) grant funded by the Korean government (MSIT) (NRF-2021R1A2C1013761 and NRF-2021R1A2C3010989), Republic of Korea. GK and JN are supported by Fermi Research Alliance, LLC under Contract DEAC02-07CH11359 with the U.S. Department of

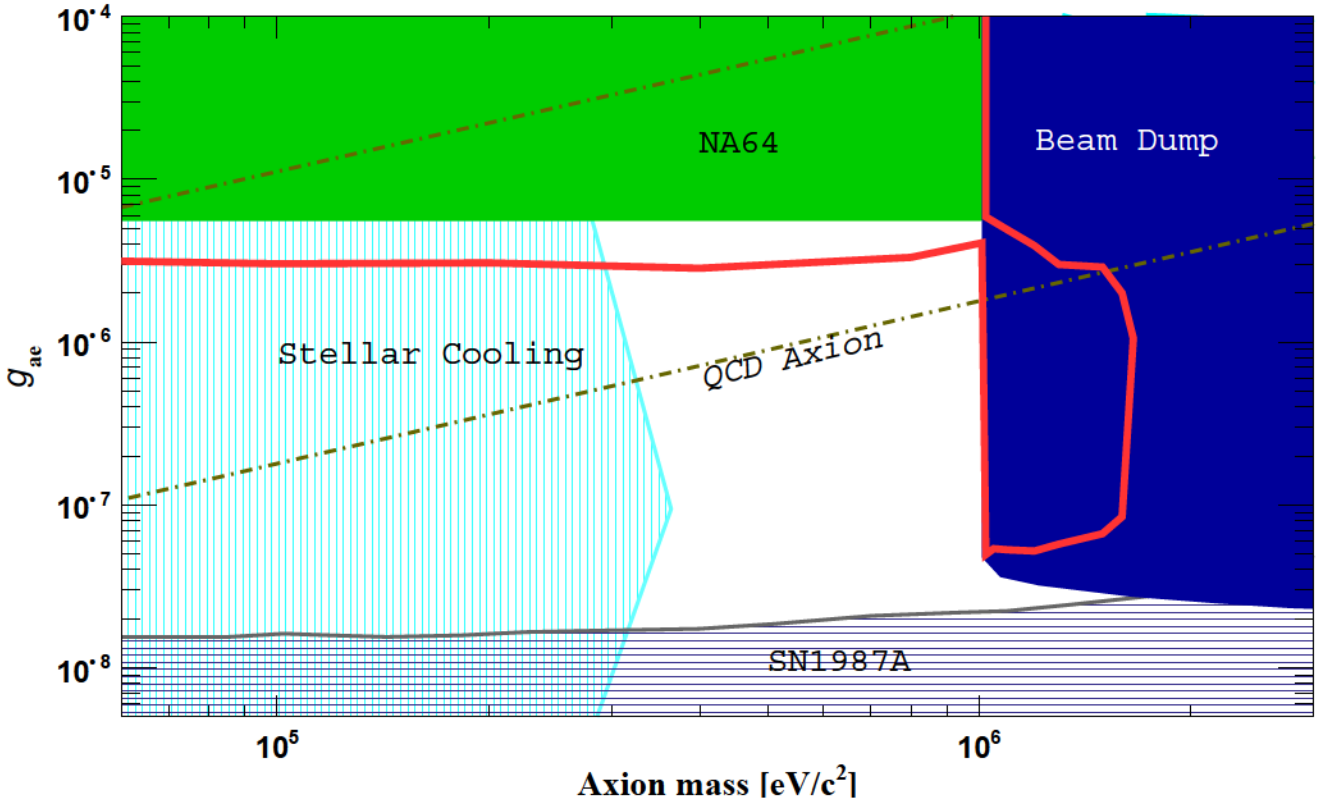


Fig. 16. Exclusion limit on the axion-electron coupling. The observed 95% confidence level exclusion limit (red solid line) on the axion-electron coupling derived from NEON data is compared with limits from beam dump experiments [68–70], SN1987A [71], stellar cooling constraints [72], and the NA64 missing energy search [73]. The QCD axion model parameter space for the DFSZ(I) benchmark scenario is indicated by the gray dashed lines [61]. This limit partially covers previously unconstrained regions of the QCD axion parameter space for axion masses around a few  $100 \text{ keV}/c^2$ .

Energy and the Kavli Institute for Cosmological Physics at

the University of Chicago through an endowment from the Kavli Foundation and its founder Fred Kavli.

- 
- [1] R. D. Peccei and H. R. Quinn, CP Conservation in the Presence of Instantons, *Phys. Rev. Lett.* **38**, 1440–1443 (1977).
  - [2] F. Wilczek, Problem of Strong  $P$  and  $T$  Invariance in the Presence of Instantons, *Phys. Rev. Lett.* **40**, 279–282 (1978).
  - [3] S. Weinberg, A New Light Boson?, *Phys. Rev. Lett.* **40**, 223–226 (1978).
  - [4] J. E. Kim, Weak Interaction Singlet and Strong CP Invariance, *Phys. Rev. Lett.* **43**, 103 (1979).
  - [5] M. A. Shifman, A. I. Vainshtein, and V. I. Zakharov, Can Confinement Ensure Natural CP Invariance of Strong Interactions?, *Nucl. Phys. B* **166**, 493–506 (1980).
  - [6] J. Preskill, M. B. Wise, and F. Wilczek, Cosmology of the Invisible Axion, *Phys. Lett. B* **120**, 127–132 (1983).
  - [7] L. F. Abbott and P. Sikivie, A Cosmological Bound on the Invisible Axion, *Phys. Lett. B* **120**, 133–136 (1983).
  - [8] M. Dine and W. Fischler, The Not So Harmless Axion, *Phys. Lett. B* **120**, 137–141 (1983).
  - [9] C. Bartram et al., (ADMX Collaboration), Search for Invisible Axion Dark Matter in the  $3.3\text{--}4.2 \mu\text{eV}$  Mass Range, *Phys. Rev. Lett.* **127**, 261803 (2021).
  - [10] K. M. Backes et al., (HAYSTAC Collaboration), A quantum-enhanced search for dark matter axions, *Nature* **590**, 238–242 (2021).
  - [11] O. Kwon et al., (CAPP Collaboration), First Results from an Axion Haloscope at CAPP around  $10.7 \mu\text{eV}$ , *Phys. Rev. Lett.* **126**, 191802 (2021).
  - [12] R. L. Workman et al., (Particle Data Group Collaboration), Review of Particle Physics, *PTEP* **2022**, 083C01 (2022).
  - [13] E. Witten, Some Properties of  $O(32)$  Superstrings, *Phys. Lett. B* **149**, 351–356 (1984).
  - [14] K. Choi, S. H. Im, and C. Sub Shin, Recent Progress in the Physics of Axions and Axion-Like Particles, *Ann. Rev. Nucl. Part. Sci.* **71**, 225–252 (2021).
  - [15] Y. K. Semertzidis and S. Youn, Axion dark matter: How to see it?, *Sci. Adv.* **8**, abm9928 (2022).
  - [16] F. Capozzi, B. Dutta, G. Gurung, W. Jang, I. M. Shoemaker, A. Thompson, and J. Yu, New constraints on ALP couplings to electrons and photons from ArgoNeuT and the MiniBooNE

- beam dump, Phys. Rev. D **108**, 075019 (2023).
- [17] G. G. Raffelt, Astrophysical axion bounds, Lect. Notes Phys. **741**, 51–71 (2008).
- [18] A. Caputo and G. Raffelt, Astrophysical Axion Bounds: The 2024 Edition, PoS **COSMICWISPer**, 041 (2024).
- [19] V. Brdar, B. Dutta, W. Jang, D. Kim, I. M. Shoemaker, Z. Tabrizi, A. Thompson, and J. Yu, Axionlike Particles at Future Neutrino Experiments: Closing the Cosmological Triangle, Phys. Rev. Lett. **126**, 201801 (2021).
- [20] G. Lucente, O. Straniero, P. Carenza, M. Giannotti, and A. Mirizzi, Constraining Heavy Axionlike Particles by Energy Deposition in Globular Cluster Stars, Phys. Rev. Lett. **129**, 011101 (2022).
- [21] P. F. Depta, M. Hufnagel, and K. Schmidt-Hoberg, Updated BBN constraints on electromagnetic decays of MeV-scale particles, JCAP **04**, 011 (2021).
- [22] A. Caputo, G. Raffelt, and E. Vitagliano, Muonic boson limits: Supernova redux, Phys. Rev. D **105**, 035022 (2022).
- [23] J. B. Dent, B. Dutta, D. Kim, S. Liao, R. Mahapatra, K. Sinha, and A. Thompson, New directions for axion searches via scattering at reactor neutrino experiments, Phys. Rev. Lett. **124**, 211804 (2020).
- [24] D. Aristizabal Sierra, V. De Romeri, L. J. Flores, and D. K. Papoulias, Axionlike particles searches in reactor experiments, JHEP **03**, 294 (2021).
- [25] A. A. Aguilar-Arevalo et al., (CCM Collaboration), Prospects for detecting axionlike particles at the Coherent CAPTAIN-Mills experiment, Phys. Rev. D **107**, 095036 (2023).
- [26] S.-H. Seo et al., Physics Potential of a Few Kiloton Scale Neutrino Detector at a Deep Underground Lab in Korea, arXiv:2309.13435.
- [27] H. M. Chang et al., (TEXONO Collaboration), Search of axions at the Kuo-Sheng nuclear power station with a high-purity germanium detector, Phys. Rev. D **75**, 052004 (2007).
- [28] S. Sahoo, S. Verma, M. Mirzakhani, N. Mishra, A. Thompson, S. Maludze, R. Mahapatra, and M. Platt, Reactor-based Search for Axion-Like Particles using CsI(Tl) Detector, arXiv:2407.14704.
- [29] J. J. Choi et al., (NEON Collaboration), Exploring coherent elastic neutrino-nucleus scattering using reactor electron antineutrinos in the NEON experiment, Eur. Phys. J. C **83**, 226 (2023).
- [30] Y. J. Ko et al., (NEOS Collaboration), Sterile Neutrino Search at the NEOS Experiment, Phys. Rev. Lett. **118**, 121802 (2017).
- [31] Y. Ko et al., NEOS Experiment, J. Phys. Conf. Ser. **1216**, 012004 (2019).
- [32] Y. J. Ko et al., (NEOS Collaboration), Comparison of fast neutron rates for the NEOS experiment, J. Korean Phys. Soc. **69**, 1651–1655 (2016).
- [33] J. J. Choi et al., (NEON Collaboration), Upgrade of the NaI(Tl) crystal encapsulation for the NEON experiment, JINST **19**, P10020 (2024).
- [34] J. J. Choi, B. J. Park, C. Ha, K. W. Kim, S. K. Kim, Y. D. Kim, Y. J. Ko, H. S. Lee, S. H. Lee, and S. L. Olsen, Improving the light collection using a new NaI(Tl) crystal encapsulation, Nucl. Instrum. Meth. A **981**, 164556 (2020).
- [35] G. Adhikari et al., (COSINE-100 Collaboration), The COSINE-100 Data Acquisition System, JINST **13**, P09006 (2018).
- [36] G. Adhikari et al., (COSINE-100 Collaboration), Background modeling for dark matter search with 1.7 years of COSINE-100 data, Eur. Phys. J. C **81**, 837 (2021).
- [37] L. Swiderski, Response of doped alkali iodides measured with gamma-ray absorption and Compton electrons, Nucl. Instrum. Meth. A **705**, 42 (2013).
- [38] S. M. Lee et al., (COSINE-100 Collaboration), Nonproportionality of NaI(Tl) scintillation detector for dark matter search experiments, Eur. Phys. J. C **84**, 484 (2024).
- [39] G. Adhikari et al., (COSINE-100 Collaboration), Lowering the energy threshold in COSINE-100 dark matter searches, Astropart. Phys. **130**, 102581 (2021).
- [40] J. J. Choi et al., First Direct Search for Light Dark Matter Using the NEON Experiment at a Nuclear Reactor, arXiv:2407.16194.
- [41] J. Amaré, S. Cebrián, C. Cuesta, E. García, C. Ginestra, M. Martínez, M. Oliván, Y. Ortigoza, A. O. de Solórzano, C. Pobes, J. Puimedón, M. Sarsa, J. Villar, and P. Villar, Cosmogenic radionuclide production in nai(tl) crystals, JCAP **2015**, 046 (2015).
- [42] P. Villar, J. Amaré, S. Cebrián, I. Coarasa, E. García, M. Martínez, M. A. Oliván, Y. Ortigoza, A. Ortiz de Solórzano, J. Puimedón, M. L. Sarsa, and J. A. Villar, Study of the cosmogenic activation in nai(tl) crystals within the anais experiment, Int. J. Mod. Phys. A **33**, 1843006 (2018).
- [43] E. Barbosa de Souza et al., (COSINE-100 Collaboration), Study of cosmogenic radionuclides in the COSINE-100 NaI(Tl) detectors, Astropart. Phys. **115**, 102390 (2020).
- [44] X. Li, B. Zheng, Y. Wang, and X. Wang, A study of daily and seasonal variations of radon concentrations in underground buildings, J. Environ. Radioact. **87**, 101–106 (2006).
- [45] C. Ha et al., Radon concentration variations at the Yangyang underground laboratory, Front. in Phys. **10**, 1030024 (2022).
- [46] P. Adhikari et al., (COSINE-100 Collaboration), Background model for the NaI(Tl) crystals in COSINE-100, Eur. Phys. J. C **78**, 490 (2018).
- [47] G. H. Yu et al., (COSINE-100 Collaboration), Improved background modeling for dark matter search with COSINE-100, arXiv:2408.09806.
- [48] M. Wojcik, W. Wlazlo, G. Zuzel, and G. Heusser, Radon diffusion through polymer membranes used in the solar neutrino experiment Borexino, Nucl. Instrum. Meth. A **449**, 158–171 (2000).
- [49] M. Roos, Sources of gamma radiation in a reactor core, J. Nucl. Energy Part B. Reactor Technol. **1**, 98–104 (1959).
- [50] H. Bechteler, H. Faissner, R. Yogeshwar, and H. Seyfarth, The spectrum of  $\gamma$  radiation emitted in the FRJ-1 (Merlin) reactor core and moderator region, 1984. Juel-Spez-255.
- [51] A. Arvanitaki, S. Dimopoulos, S. Dubovsky, N. Kaloper, and J. March-Russell, String axiverse, Phys. Rev. D **81**, 123530 (2010).
- [52] M. Cicoli, M. D. Goodsell, and A. Ringwald, The type IIB string axiverse and its low-energy phenomenology, JHEP **2012**, 146 (2012).
- [53] H. Primakoff, Photo-production of neutral mesons in nuclear electric fields and the mean life of the neutral meson, Phys. Rev. **81**, 899–899 (1951).
- [54] Xcom: Photon cross sections database, <https://www.nist.gov/pml/xcom-photon-cross-sections-database>. Accessed: 2024-12-09.
- [55] F. T. Avignone III, R. L. Brodzinski, S. Dimopoulos, G. D. Starkman, A. K. Drukier, D. N. Spergel, G. Gelmini, and B. W. Lynn, Laboratory Limits on Solar Axions From an Ultralow Background Germanium Spectrometer, Phys. Rev. D **35**, 2752 (1987).

- [56] G. Bellini et al., Search for solar axions emitted in the M1-transition of  ${}^7\text{Li}^*$  with Borexino CTF, *Eur. Phys. J. C* **54**, 61–72 (2008).
- [57] L. Lyons, Raster scan or 2-D approach?, [arXiv:1404.7395](https://arxiv.org/abs/1404.7395).
- [58] G. Adhikari et al., (COSINE-100 Collaboration), Search for Boosted Dark Matter in COSINE-100, *Phys. Rev. Lett.* **131**, 201802 (2023).
- [59] J.-F. Fortin, H.-K. Guo, S. P. Harris, D. Kim, K. Sinha, and C. Sun, Axions: From magnetars and neutron star mergers to beam dumps and BECs, *Int. J. Mod. Phys. D* **30**, 2130002 (2021).
- [60] B. Batell et al., Dark Sector Studies with Neutrino Beams, in *Snowmass 2021*, 7, 2022. [arXiv:2207.06898](https://arxiv.org/abs/2207.06898).
- [61] L. Di Luzio, M. Giannotti, E. Nardi, and L. Visinelli, The landscape of QCD axion models, *Phys. Rept.* **870**, 1–117 (2020).
- [62] J. Jaeckel and M. Spannowsky, Probing MeV to 90 GeV axion-like particles with LEP and LHC, *Phys. Lett. B* **753**, 482–487 (2016).
- [63] J. Blumlein et al., Limits on the mass of light (pseudo)scalar particles from Bethe-Heitler e+e- and mu+mu- pair production in a proton - iron beam dump experiment, *Int. J. Mod. Phys. A* **7**, 3835–3850 (1992).
- [64] A. Payez, C. Evoli, T. Fischer, M. Giannotti, A. Mirizzi, and A. Ringwald, Revisiting the SN1987A gamma-ray limit on ultralight axion-like particles, *JCAP* **02**, 006 (2015).
- [65] J. Jaeckel, P. C. Malta, and J. Redondo, Decay photons from the axionlike particles burst of type II supernovae, *Phys. Rev. D* **98**, 055032 (2018).
- [66] M. J. Dolan, T. Ferber, C. Hearty, F. Kahlhoefer, and K. Schmidt-Hoberg, Revised constraints and Belle II sensitivity for visible and invisible axion-like particles, *JHEP* **12**, 094 (2017). [Erratum: *JHEP* 03, 190 (2021)].
- [67] P. Carenza, O. Straniero, B. Döbrich, M. Giannotti, G. Lucente, and A. Mirizzi, Constraints on the coupling with photons of heavy axion-like-particles from Globular Clusters, *Phys. Lett. B* **809**, 135709 (2020).
- [68] J. D. Bjorken, S. Ecklund, W. R. Nelson, A. Abashian, C. Church, B. Lu, L. W. Mo, T. A. Nunamaker, and P. Rassmann, Search for Neutral Metastable Penetrating Particles Produced in the SLAC Beam Dump, *Phys. Rev. D* **38**, 3375 (1988).
- [69] D. J. Bechis, T. W. Dombeck, R. W. Ellsworth, E. V. Sager, P. H. Steinberg, L. J. Teig, J. K. Yoh, and R. L. Weitz, Search for Axion Production in Low-energy Electron Bremsstrahlung, *Phys. Rev. Lett.* **42**, 1511 (1979). [Erratum: *Phys. Rev. Lett.* **43**, 90 (1979)].
- [70] E. M. Riordan et al., A Search for Short Lived Axions in an Electron Beam Dump Experiment, *Phys. Rev. Lett.* **59**, 755 (1987).
- [71] G. Lucente and P. Carenza, Supernova bound on axionlike particles coupled with electrons, *Phys. Rev. D* **104**, 103007 (2021).
- [72] E. Hardy and R. Lasenby, Stellar cooling bounds on new light particles: plasma mixing effects, *JHEP* **02**, 033 (2017).
- [73] S. N. Gninenko, D. V. Kirpichnikov, M. M. Kirsanov, and N. V. Krasnikov, The exact tree-level calculation of the dark photon production in high-energy electron scattering at the CERN SPS, *Phys. Lett. B* **782**, 406–411 (2018).